Acta Materialia 120 (2016) 24–31

Contents lists available at ScienceDirect

Acta Materialia

journal homepage: www.elsevier.com/locate/actamat

Full length article

A principle curvatures analysis of the isothermal evolution of nanoporous gold: Quantifying the characteristic length-scales

Markus Ziehmer [a, *], Kaixiong Hu [a], Ke Wang [b], Erica T. Lilleodden [a]

[a] Helmholtz-Zentrum Geesthacht HZG, Institut für Werkstoffforschung, Werkstoffmechanik, 21502, Geesthacht, Germany
[b] Technische Universität Hamburg, Institut für Werkstoffphysik und -technologie, 21073, Hamburg, Germany

ARTICLE INFO

Article history:
Received 22 March 2016
Received in revised form
7 July 2016
Accepted 12 August 2016
Available online 29 August 2016

Keywords:
Nanoporous gold
Principle curvatures
Microstructure evolution
Focused ion beam tomography
Self-similarity

ABSTRACT

A study of the isothermal evolution of a nanoporous gold (npg) microstructure after dealloying has been performed. In order to adequately characterize its complex three-dimensional bicontinuous ligament-ring structure, an analysis of the scaled principle curvatures κ_1 and κ_2 based on representative volumes of meshed 3D reconstructions was applied. Five npg samples, as obtained from an electrolytical dealloying process, with different mean ligament diameters ranging from ca. 25 nm (as-dealloyed) to ca. 420 nm (from annealing at 300° C) were analyzed. The results indicate that ligament surface flattening effects lead to small but distinct morphological changes during the investigated early and mid-stages of coarsening, visible in the scaled κ_1- and κ_2- marginal distributions. Thus, strictly speaking, self-similar evolution of npg cannot be confirmed, but dependent on the specific application, the evolution might be seen as "sufficiently" self-similar. Moreover, it is shown that the inverse mean principle curvatures from the marginal distributions can be used to identify the mean sizes of the two salient structural features, namely the ligaments and the rings. Both inverse mean principle curvatures scale linearly with the mean ligament diameter. Thus, for the material used in this study, one parameter is sufficient to characterize its microstructure. Finally, it is shown that rings resembling the ones from the real samples can be generated computationally by applying modified torus parameterizations. Surprisingly, a calculation of the curvature distribution of only one "average" ring is sufficient to approximate the scaled kappa distributions accumulated from the ring distributions of the real samples.

1. Introduction

Apart from purely academic interest, microstructure evolution has provided attraction for materials science research ever since it was recognized that technologically interesting properties can be tailored via growth or coarsening of salient microstructural features such as grains in polycrystals. Mathematically, the link between some specific property and the structural sizes is often given as a scaling law. One prominent example is the Hall-Petch law that relates the yield stress of a coarse-grained material to the inverse square root of the mean grain size, see e.g. Ref. [1]. Implicitly, the validity of such a scaling law is founded by the self-similarity of an underlying phenomenon, grain growth in the given example. Loosely speaking, self-similarity implies "an object looks roughly the same on any scale" (from Wolfram Mathworld, http://mathworld.wolfram.com/Self-Similarity.html). Translated into a mathematical language and illustrated e.g. by growth and coarsening processes like normal grain growth or Ostwald ripening it means that the size distributions resulting from an isothermal evolution process are time-invariant upon scaling by the respective mean structural sizes [2,3].

While the examples given above describe systems which are typically characterized by one size measure, e.g. the mean grain size or mean particle size, there are microstructures exhibiting a much stronger three-dimensional morphological and topological complexity. The structural sizes of such systems might not be characterized sufficiently by only one metric. Nanoporous gold (npg), a material that gained considerable interest in the past decade, is one example of such a material. Its microstructure is usually described as a 3D bicontinuous, interconnected pore-ligament network with a typical initial mean ligament diameter of about 5–50 nm, depending on the dealloying conditions [4]. However, it appears to be more appropriate to call it a ligament-ring structure, since essentially two distinct morphologies can be

* Corresponding author.
E-mail address: markus.ziehmer@hzg.de (M. Ziehmer).

http://dx.doi.org/10.1016/j.actamat.2016.08.028

discriminated (Fig. 1): the ligaments themselves and the irregular shaped, torus-like rings formed by the interconnected ligaments. Thus, the ligament and the ring diameters might be seen as the two fundamental metrics of npg. It should be noted that both of these structural features can have a distinctly different impact on the mechanical properties of npg. It is still unclear, if there is a correlation between these two mean sizes that might or might not be maintained during coarsening.

Structural coarsening of npg can be easily achieved via thermal annealing after dealloying, thereby increasing the ligament sizes as well as the ring sizes. This requires a reduction of the number of rings per unit volume over time while keeping the solid volume fraction constant. This means that in order to make self-similar coarsening of both ligaments and rings possible, rings must be opened. So-called pinch-off events have been proposed [5], which are necessary for a self-similar evolution of the topology of such a bicontinuous network structure [6]. Dead-end ligaments resulting from these events can be found in the microstructure throughout the coarsening process (see Fig. 1c and d). This is of great importance for mechanical applications, since dead-end ligament parts do not contribute to the load bearing parts of the npg network [7].

Experimentally, Chen-Wiegart et al. concluded that npg does not coarsen in a self-similar manner [8], based on their results of the isothermal temporal evolution of the inverse specific surface area, and of the evolution of the surface principle curvatures κ_1 and κ_2, represented as so-called 2D scaled interface shape distributions (ISD). ISD's have already been used to characterize systems with complex microstructures, see e.g. Refs. [9,10], because direct access to 3D size distributions of the structural constituents was not possible. The scaled ISD's shown in Chen-Wiegart's work are clearly not time-invariant, and the explanation they give relates to a seemingly increasing anisotropy of the npg microstructure. However, it appears that the X-ray nanotomography approach taken to reconstruct the 3D structure negates volumes which can be considered as representative during the later annealing stages. We have already demonstrated the importance of using representative volumes in analyzing the npg microstructure [7]. It was shown that the side length of the representative cube volumes scaled with the mean ligament diameters by a factor of about 14–16 for the electrolytically dealloyed bulk npg samples used. On the other hand, it is unclear to what extent the various sample preparation steps, i.e. preparation of the AgAu alloy and dealloying, influence the resultant, as-dealloyed structure. The self-similar regime might be attained only in later coarsening stages, where Chen-Wiegart et al. are critically limited in the volumes analyzed. It has to be mentioned that Chen-Wiegart applied a free corrosion process to produce the npg samples which might yield different as-dealloyed structures than the ones from an electrolytical dissolution process.

Computationally, it was shown that bicontinuous structures, qualitatively resembling npg structures, can be generated by employing phase field spinodal decomposition [9]. Investigation of the structural evolution showed that self-similarity well describes late-stage coarsening via conserved dynamics of samples with a solid volume fraction of 36% [6].

We propose analyzing representative volumes and extending the surface curvature analysis by making use of not just only the 2D ISD representations but of the marginal κ_1- and κ_2-distributions as well. This approach is based on the assumption that the two basic npg microstructure constituents, rings and ligaments, are each representable by one of the two principle curvatures κ_1 and κ_2 respectively. This is identically the case for a regular torus surface, see Fig. 2, recognizing that for a regular torus κ_2 (due to our choice) exclusively reflects the inverse ligament radius, because $\kappa_1<\kappa_2$ always, due to $\mathrm{Max}(\kappa_1)=1/(R+r)<1/r$. Since the torus is a closed ring, the mean of the second principle curvature value $\langle\kappa_1\rangle$ is negative, and reflects the ring size in some way. If we consider the real npg microstructure to be built up by interconnected tori, each on average contributing by only half of its volume, the splitting of the two principle curvatures is even clearer, because κ_1 is mostly negative, reflecting the ring characteristics. Consequently, if the single principle curvatures are believed to reflect different structural features, then the 2D distributions can be split into the marginal κ_1- and κ_2-distributions, such that the ring and ligament characteristics are independently given. Though it is questionable in how far these two distributions reflect the "true" 3D ligament and ring diameter distributions, information about the mean ligament and ring sizes might be extracted from the inverse mean principle curvatures $\langle\kappa_1\rangle^{-1}$ and $\langle\kappa_2\rangle^{-1}$. Of course, the influence of the irregularities of the real rings, e.g. aspect ratios of the two main ring axes, have to be taken into account, which can be done by

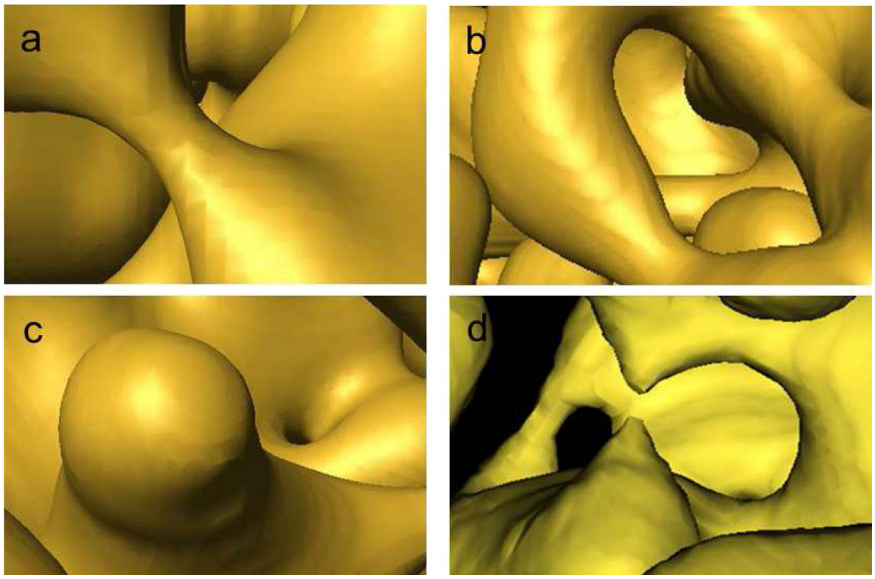

Fig. 1. Snapshots from a 3D FIB tomography reconstruction of a npg sample with mean ligament diameter of about 420 nm. The images reflect the typical structural features visible in all samples: (a) single ligaments that are connected to (b) irregular tori, which are sometimes opened exhibiting dead-end parts (c) and (d).

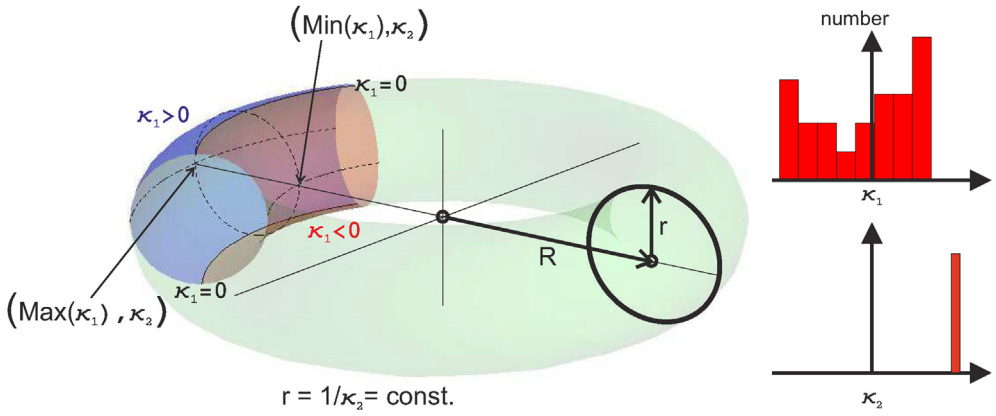

Fig. 2. Exemplification of the principle curvatures κ_1 and κ_2 of an isolated regular torus with radii r and R. A regular torus is built by saddle-shape (red, $\kappa_1<0$, $\kappa_2>0$) and convex (blue, $\kappa_1>0$, $\kappa_2>0$) surface patches, with separating infinitesimal cylindrical patches (two black lines, $\kappa_1=0$, $\kappa_2>0$) in between. The dashed lines show the two principle directions at the points (Max(κ_1),κ_2) and (Min(κ_1),κ_2). While $\kappa_2=1/r$ is constant and positive, κ_1 lies in the interval [Min(κ_1)$=-1/(R-r)$, Max(κ_1)$=1/(R+r)$]. An analysis of the two marginal κ-distributions yield histograms like shown. Note that κ_1 is always smaller than κ_2 since Max(κ_1)$=1/(R+r)<\kappa_2=1/r$. (For interpretation of the references to colour in this figure legend, the reader is referred to the web version of this article.)

analytically examining principal curvature distributions. Moreover, interconnecting elements and dead-end ligaments in particular, e.g. Fig. 1(c), are likely to add convex surface contributions to the curvature distributions. This would lead to a shift toward more positive κ_1-values. This is discussed further below.

2. Experimental and analyses

Experimentally, our study relies on 3D reconstructions of representative volumes from focused ion beam (FIB) tomography of five epoxy-infiltrated samples used in Ref. [7] with mean ligament diameters $\langle D\rangle_{lig}$ of ca. 26 nm (as-dealloyed), 44 nm, 208 nm, 369 nm, and 418 nm (from annealing at temperature T = 300° C for 2, 30, 240 and 420 min respectively). The $\langle D\rangle_{lig}$ values were achieved from 3D ligament diameter distributions, generated by applying a method introduced by Hildebrand et al. [11] and implemented in a Fiji plug-in [12]. Briefly, this method calculates, for each voxel in the object of interest (i.e the Au ligament network), the diameter of the largest sphere that fits into the structure of interest and contains the specific voxel. From this analysis, histograms were constructed that could be fitted by Gauss distributions (not shown here). The mean ligament diameters given in this text were calculated as the averages taken from six different regions for each of the five samples.

Since FIB tomography is destructive by nature, it was necessary to use several samples in order to follow the coarsening behavior of the npg microstructure. The samples were made from an Ag_{75} Au_{25} alloy, resulting in solid volume fractions of 29.6% (as-dealloyed), 30.4%, 30.9%, 35.5%, and 33.4% (2, 30, 240, and 420 min annealed), as analyzed from the reconstructed volumes. More details regarding sample fabrication can be found in Ref. [13].

The 3D reconstructions were achieved from an automatized sequential milling and imaging procedure performed with a Nanolab 200 dualbeam SEM and focused ion beam (FIB) microscope (FEI Corp.), making use of its “Auto Slice and View” software. Details of such a tomographic approach can be found elsewhere, e.g. Ref. [14]. Instead of milling the open-porous npg structures, which can lead to redeposition within the pores, we benefitted from infiltrating the pore structure with an epoxy polymer, which facilitates clean cross-sectioning of npg. Due to the comparably low secondary electron yield of the epoxy phase, this special two-phase composite material allowed for adjusting the SEM imaging parameters in a way that simplified the segmentation process. Adjusting the brightness and contrast values of the in-the-lens secondary electron detector allowed for sampling raw images almost being binary. Typical electron beam parameters employed were 2 kV high voltage and 0.21–0.54 nA beam currents, and ion beam parameters used for slicing were 30 kV and 0.1–0.3 nA. Fig. 3 shows a typical image taken during slicing of the as-dealloyed sample. The block of material to be sliced with a Pt layer on top

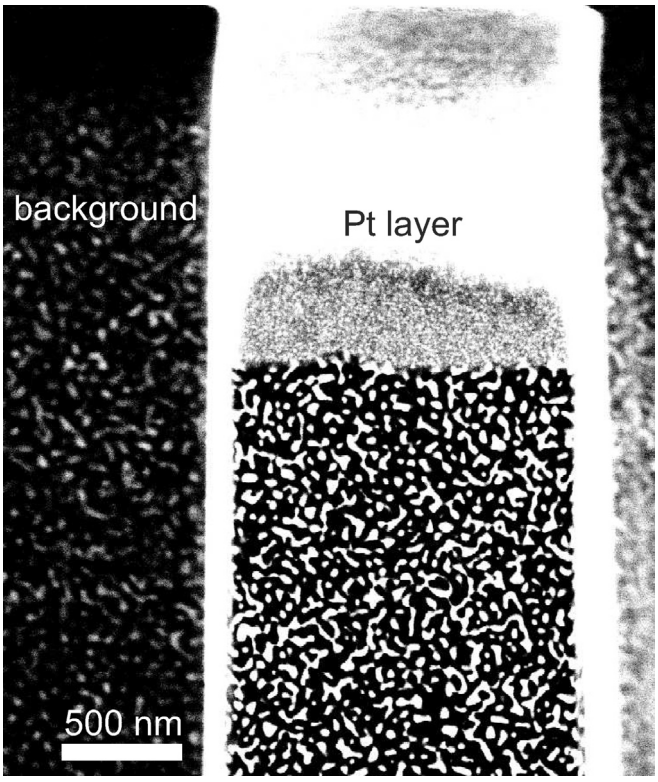

Fig. 3. Typical SEM secondary electron micrograph from sectioning the as-dealloyed sample. The block of material to be sliced can be easily recognized. The Pt layer on top facilitated clean FIB cross-sectioning. Adjustment of the brightness and contrast values before starting the automated slicing and imaging process enabled getting raw images that were easy to binarize in the final segmentation process. As can be seen, the ligament sections that appear bright are clearly differentiated from the epoxy phase appearing dark. Pixel size in this image is 3.6· 3.6 nm^2

can be easily recognized, as well as part of the trench besides. The gold phase is represented as bright and the epoxy phase as dark. With this approach, the subsequent binarization could be easily performed in Fiji. Finally, registration of the image stack was performed by a subpixel registration algorithm, using a Fiji plugin called "stackreg registration", which is based on grayscale intensity of the image stack. The 3D visualization can be performed both by the Fiji and Amira 4.1 software. Free-floating ligament sections appearing at the edges of the reconstructions were removed. The volume fractions of these were typically less than 2% of the total solid volume fractions.

Naturally, the as-dealloyed sample ($\langle D\rangle_{lig} \approx 26$ nm) and the sample from the first annealing step ($\langle D\rangle_{lig} \approx 44$ nm) are by far the most critical ones to be reconstructed. While lateral (x-y) resolution is not such a major issue, slicing distance is. With decreasing structural sizes, the ratio of the mean structural sizes to the mean slice distance decreases upon approaching the limits of the method, thereby increasing errors. For our reconstructions, we used a mean slice distance as an input, determined as the ratio of the final total sliced distance to the number of slices, typically 500. In this way, the ratio of mean ligament diameter to voxel dimension increased from around 8 for the samples with the smallest $\langle D\rangle_{lig}$ to around 20 for the samples with the larger structural sizes, with voxel sizes in the range of $4 \cdot 4 \cdot 3$ nm^3 to $18 \cdot 18 \cdot 23$ nm^3. Mangipudi et al. [15] presented a detailed analysis on the question of processing errors introduced to reconstructions of as-dealloyed npg through the use of constant slice thicknesses. The ISDs they present show that there are small but distinct differences between assuming a constant slice thickness rather than using the actual slice thicknesses (see Fig. 7 therein).

The curvature analysis was accomplished on triangulated meshes of the reconstructed representative volumes. The meshes were generated by the Amira 4.1 software, having the option to specify the number of nodes, and thus triangles, employed. Care has been taken to make sure that the npg reconstructions were adequately meshed, i.e. the number of nodes used must have been large enough to smoothly reproduce the very high curvature regions inherent in npg. A typical example of the dependency of scaled κ marginal distributions on the number of mesh nodes is given in Fig. 4. As expected, if the node number is too low, the high curvature regions are not reflected; at a certain number of nodes, the distribution reaches a constant state (100,000 in the example here), indicating the reliability of the used mesh.

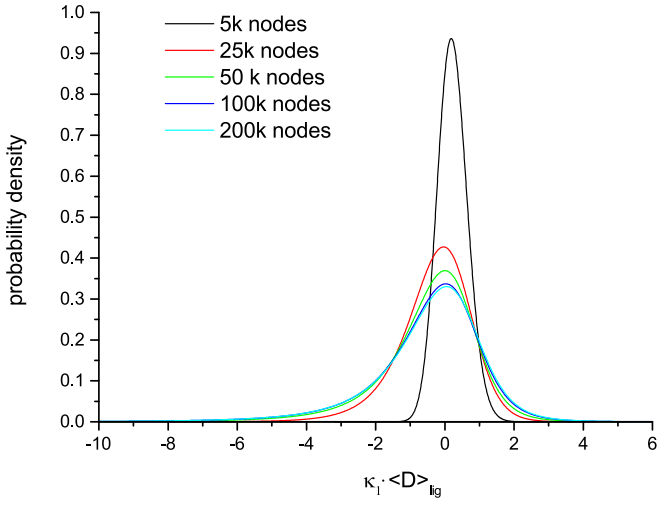

Fig. 4. In order to identify a sufficient number of triangles and thus nodes in the meshes used, visual and quantitative inspection were performed. The plot shows the typical evolution of the marginal distributions with increasing number of nodes, in this example, a scaled κ_1 marginal distribution of one sample. Clearly, a certain number is needed to make the distribution constant; here the 200,000 nodes distribution is practically identical to the 100,000 nodes distribution.

In order to calculate the principle curvature values we applied the so-called parallel surface method, introduced elsewhere [16,17]. Very briefly, this method calculates the mean and the Gauss curvatures, H and K, respectively, of one-ring neighborhoods around each mesh node from which the (κ_1,κ_2)-pairs can be computed. The node coordinates together with the node number triplets that define the mesh triangles were used as inputs for the curvature calculations. The results were scaled by the mean ligament diameters $\langle D\rangle_{lig}$ given above, and subsequently used to construct histograms, either as 2D scaled (κ_1,κ_2)-histograms or as marginal histograms. The histograms were normalized in order to end up with probability density plots. The marginal histograms could be nicely fitted by Pearson IV fit functions. The analysis was carried out on six regions each sample, and the averaged fits for each sample were calculated. Since the differences between the different regions were rather small, the contour plots shown here are taken from only one region of either sample.

Finally, we applied results from differential geometry to parametric equations of torus surfaces to compute (κ_1,κ_2)-distributions analytically. This approach enabled gaining insight into possible consequences of the irregular tori shapes on the (κ_1,κ_2)-distributions compared to regular tori. A regular torus can be generated by applying the following parameterization:

$$\begin{aligned} x &= x(\varphi,\vartheta) = (R + r\cos\varphi)\sin\vartheta, \\ y &= y(\varphi,\vartheta) = (R + r\cos\varphi)\cos\vartheta, \\ z &= z(\varphi,\vartheta) = r\sin\varphi, \end{aligned} \tag{1}$$

with φ,ϑ running from 0 to 2π, and r and R as defined in Fig. 2. This parameterization can be easily extended to produce irregular shaped tori, by introducing two ring radii $R_{1,2}$ with ratios $R_1/R_2 \neq 1$ or modulations of the ligament diameter.

The curvature properties of such surfaces can then be computed by applying the fundamental forms of differential geometry which serve to define the metric and curvature properties of a surface. This can be found in textbooks, e.g. Ref. [18].

3. Results and discussion

Typically, the 2D histograms of the scaled principle curvatures were quite sharply peaked, and the scaled κ_1 and κ_2 were found in intervals of roughly [−10,4] and [−1,10], respectively, with the intervals of the peak core regions being around [−2,2] and [0,4]. Due to our choice of κ_2 being the maximum curvature value, no values in the region $\kappa_2 < \kappa_1$ appear.

In order to simplify the comparibility, at first the evolution of the peak core regions are represented as 2D probability density contour plots, shown in Fig. 5. The dashed lines indicate the points with $\kappa_1 = \kappa_2$. The area fractions of saddle-shaped ($\kappa_1 < 0, \kappa_2 > 0$) and convex surface patches can be easily calculated and are given in Table 1, together with the very small amount of concave patches (κ_1,$\kappa_2 < 0$) that is not visible in the contour plots. In spite of the variations visible, the contour plots look quite similar with an apparently stationary peak position across all sizes. This in sharp contrast to the results presented in Refs. [8], in which the authors demonstrate and conclude that the structural evolution is not time-invariant, based on the scaled ISDs. Very different to both the experimental and simulation results presented in Refs. [8] and [6] from samples with solid volume fractions of 28% [8] and 36%, 40%, and 50% [6], the npg we analyzed (ca. 32% average solid volume fraction), displayed large fractions of convex surface patches (κ_1,$\kappa_2 > 0$). As a

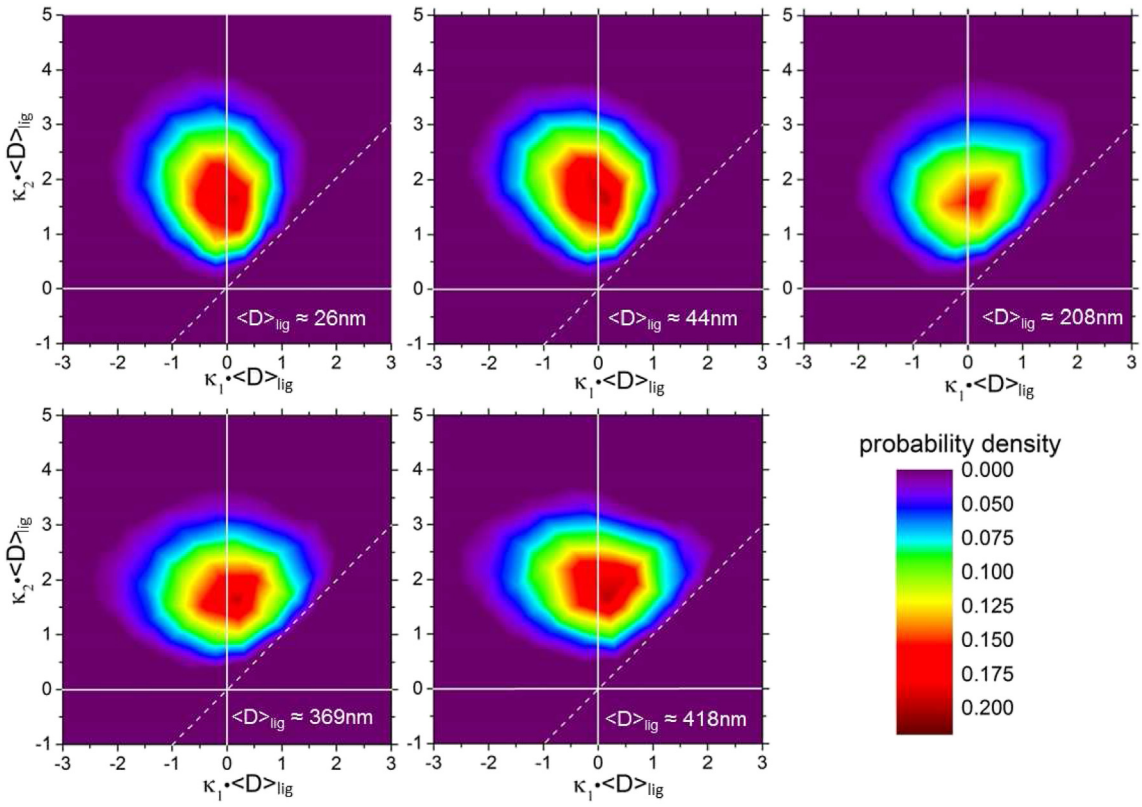

Fig. 5. 2D probability density contour plots of the scaled (κ_1,κ_2) distribution core regions of the five samples. The $\langle D\rangle_{lig}\approx$208nm sample appears to be an outlier. Otherwise, some evolution from the very early to the later stages can be seen, finally resulting in distributions almost symmetrical around κ_1=0.

Table 1
The area fractions of saddle-shape, convex and concave surface patches of the five investigated samples with mean ligament sizes $\langle D\rangle_{lig}$. It can be seen that there is a slight decrease in the saddle-shaped area fraction with an associated increase in the amount of concave surface patches. Overall, the changes are rather small and, in particular, the samples arrive at almost equal amounts of saddle-shape and convex surface patches. Some concave areas were detected too, but are negligible.

$\langle D\rangle_{lig}$	26 nm	44 nm	208 nm	369 nm	418 nm
A_{rel}^{saddle}	0.610	0.613	0.536	0.550	0.550
A_{rel}^{convex}	0.387	0.385	0.457	0.447	0.447
$A_{rel}^{concave}$	0.003	0.003	0.007	0.003	0.003

consequence, our ISDs are somewhat symmetrical around $\kappa_1\approx 0$, particularly in the later coarsening stages. The simulation results presented in Ref. [6] indicate an evolution with increasing solid volume fractions towards a symmetrical distribution centered on the scaled $\kappa_1\approx-\kappa_2$-line. Our results and the experimental results from Ref. [8] would be in line with that if not the solid volid fraction claimed in Ref. [8] would be less than ours.

If there is no fundamental difference between npg microstructures resulting from "uncontrolled" free corrosion as a dealloying procedure and "controlled" electro-chemical dealloying, the reason for this discrepancy might be found in the possibly insufficient volumes investigated there. Since we found for our systems the minimum reconstructed cube box lengths to be about $14-16\cdot\langle D\rangle_{lig}$, a reconstructed volume size of $(6.5\mu m)^3$ appears to be too small for the larger ligament sizes achieved in Ref. [8] (see Fig. 2 therein). Since the volumes investigated in Ref. [8] should have been large enough for the initial annealing steps, it seems that dealloying, and in general the whole sample processing, may lead to different structures (comparing Fig. 2(a) in Ref. [8] and our results). Then, self-similarity might be reached only at later stages of coarsening.

Fig. 6 shows the scaled marginal κ_1- and κ_2-distributions over the full data range. This kind of representation highlights the fact that the distributions are tailed which cannot be shown as clearly in the contour plots. Apart from the $\langle D\rangle_{lig}\approx$208nm outlier, both distributions exhibit clear trends, with the scaled κ_2 getting sharper and the scaled κ_1-distributions becoming broader with increasing $\langle D\rangle_{lig}$. Though the differences are small, self-similarity cannot be stated in a strict way. Keeping in mind that the FIB tomography and subsequent analyses were carried out at the nanoscale, a clear conclusion regarding the validity of describing the structure evolution as self-similar is difficult to make. In particular, the two samples with the smallest mean ligament sizes push the limits of FIB tomography in several aspects (see section 2). However, once the mean ligament sizes increase, the negative impacts of non-constant slice thicknesses and ligament-size-to-voxel-size ratio decrease.

One might wonder if the pronounced tails in the curvature distributions are artifacts from the analysis, such as the surface mesh quality or the reconstructions directly. However, this effect seems to evolve naturally from the irregularities of the npg ring structure, namely the aspect ratios of the principal ring axes in combination with ligament diameter modulations along the rings. It is fairly easy to generate rings computationally that resemble the ones found from the reconstructions of the real samples. By modifying the torus parameterization given in eqn. (1), it is possible to introduce the irregularities necessary to end up with ligament diameter modulations and ring diameter ratios $\neq 1$. By trial and error, one can even manage to generate a single average ring which reflects the curvature analysis of the real structures, depending on the range of the parameter φ in eqn. (1). Three cases are presented: $\varphi\in[\pi/2,3/2\pi]$, $\varphi\in[\pi/5,9/5\pi]$, and $\varphi\in[0,2\pi]$, the structures of which

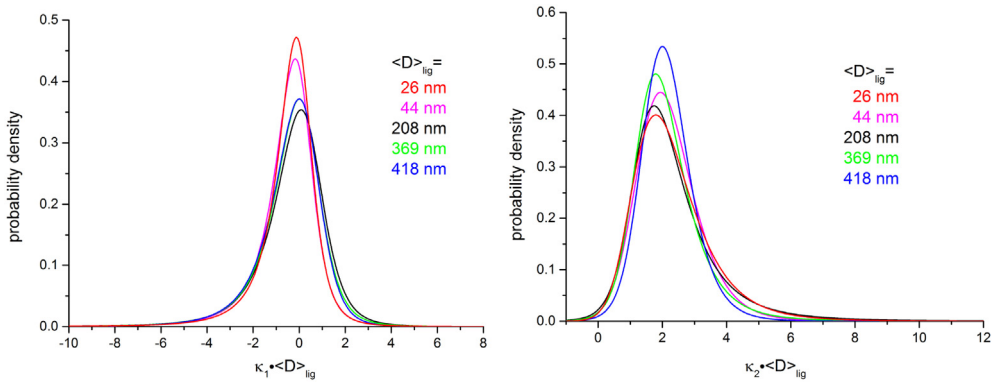

Fig. 6. The scaled marginal κ_1- (left) and κ_2- (right) probability density distributions are shown. The scaled κ_1 are fairly self-similar (note that the green curve is almost identical to the blue one and hidden behind), in contrast to the scaled κ_2-distributions, which narrow with increasing $\langle D\rangle$. (For interpretation of the references to colour in this figure legend, the reader is referred to the web version of this article.)

are shown in Fig. 7 from left to right. The corresponding analytically calculated scaled marginal distributions are shown in Fig. 8, for comparison together with the curves of the $\langle D\rangle_{lig} \approx 369$nm-sample, since the artificial ring we generated yielded a mean ligament diameter of about 330 nm.

Fig. 8 suggests that the distribution tails associated with the real samples may naturally evolve from the ring shape modulations, even if only a complete, isolated ring is considered. This should be compared to the typical κ-distributions of regular tori, shown as histograms in Fig. 2. The variation of the range of parameter φ essentially affects only the κ_1-distribution, as expected, not considering here details of the spatial arrangement of the interconnected rings in real samples. On average, each ring should contribute by half of its volume. One can see that upon approaching half of the φ range, i.e. approximately half of the ring volume, one approaches the result from the $\langle D\rangle_{lig} \approx 369$ nm-sample. It is only the largest positive values that are not reproduced by this simple approach, which we assign to interconnecting elements or dead-end ligaments in the real structures. Microstructural features like the one shown in Fig. 1 would mostly add convex surface patches to the structure (κ_1,κ_2>0), which could shift the analytical κ_1-distribution to more positive values, the extent of the shift being dependent on the amount and sizes of the features. This might better approximate the distributions of the real structures, yet was not considered further herein.

However, a surprising result might be that one single ring can almost perfectly reproduce the accumulated distributions from distributions of up to several hundred rings. This might point out that the ring size distribution in the real samples could be rather narrow. Of course, it should be noted that different 2D distributions can have identical marginals, at least in simple cases. Fig. 9 shows the 2D contour plot of the artificial average ring, which differs from the plots shown in Fig. 5 particularly in its peak height, apart from the missing positive κ_1-values. Again, it appears that the same argumentation given above should hold: adding interconnecting and dead-end microstructural elements might shift the ISD towards the real ones. Future analytical work might be aimed to reproduce the real ISD analytically, employing different ring size distributions and irregularities as well as different relative amounts of non load-bearing structural features. This has been out of scope in the work presented here.

The question remains, if and to what extent the two marginal distributions reflect the evolution of the rings and the ligaments. The same trend towards narrower distributions with increasing mean ligament size is visible both in the scaled ligament diameter distributions presented in Ref. [7] and the scaled κ_2-distributions shown here, which might be explained physically by surface flattening effects during annealing, which should not be mixed up with surface faceting, which we never detected at the low annealing temperature of 300° C within the annealing times of 2, 30, 240, and 420 min employed. Instead, we mean removal of (scaled) high curvature regions by surface diffusional mass transport. According to our working hypothesis outlined in the introduction, the scaled κ_2-distributions might be seen to mirror the ligament diameter characteristics. In order to test this hypothesis, we plotted $\langle\kappa_2\rangle^{-1}$ against $\langle D\rangle_{lig}$ shown in Fig 10. The linear fit yields $\langle\kappa_2\rangle^{-1} \approx 0.46 \cdot \langle D\rangle_{lig} \approx \langle R\rangle_{lig}$, which supports our hypothesis.

As for the ring sizes and their possible relation to the scaled κ_1, we made use of the results for the scaled connectivity densities $C_V \cdot \langle D\rangle_{lig}^3$ given in Ref. [7]. Since the connectivity density C_V reflects the number of rings per unit sample volume, it follows for the average volume per ring:

$$\langle V\rangle_{ring,1} = \rho_{solid}/C_V.$$

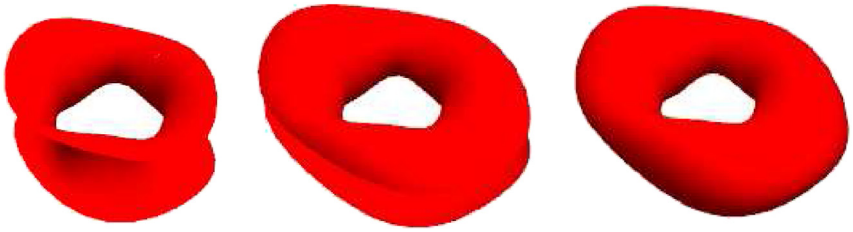

Fig. 7. Computationally generated ring, the marginal distributions of which can be very close to the results from the real structures from up to several hundred rings, depending on the range of the angle φ in the parameterization applied (see eqn. (1)), which controls the volume of the generated closed ring. An analysis were carried out for three cases, as shown here from left to right: $\varphi \in [\pi/2,3/2\pi]$, $\varphi \in [\pi/5,9/5\pi]$, and $\varphi \in [0,2\pi]$, see text.

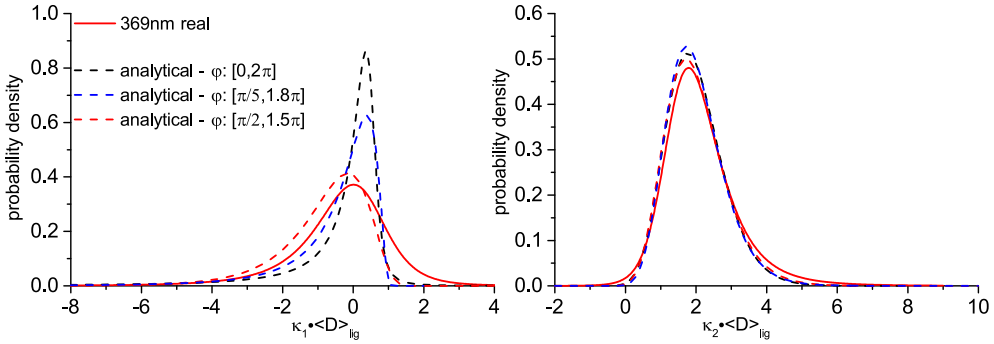

Fig. 8. The marginal κ-distributions of the ring structures shown in Fig. 7 in comparison to the results of the $\langle D\rangle_{lig} \approx$ 369nm-sample. The tails of the distributions are a natural result of the irregularities, i.e. the deviations from the regular torus shape. Reducing the range of the parameter φ (see eqn. (1)), makes the κ_1-distribution approaching the one from the real sample. As expected, the κ_2-distribution is mostly unaffected.

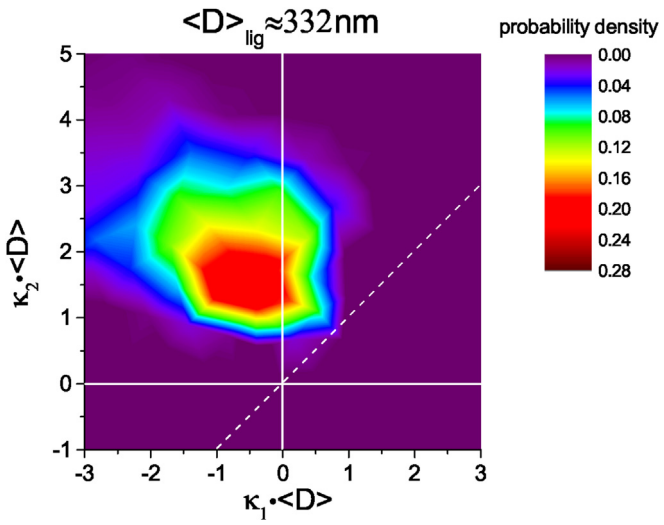

Fig. 9. 2D κ_1,κ_2-distribution contour plot of the computed half ring structure.

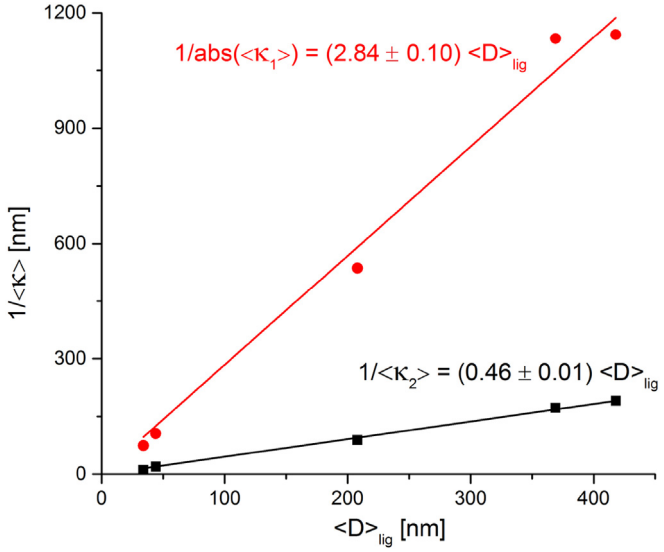

Fig. 10. Plots of the inverse mean κ against $\langle D\rangle_{lig}$. Both inverse κ exhibit a linear dependency with respect to $\langle D\rangle_{lig}$. The result from the linear fit of $1/\langle\kappa_2\rangle_{lig}$ vs. $\langle D\rangle_{lig}$ shows a very good agreement to the working hypothesis that the κ_2 reflect the ligament structure.

Using $\rho_{solid} \approx 0.3$ and $C_V \cdot \langle D\rangle_{lig}^3 \approx 0.10 - 0.11$ [7], the average ring volume can be estimated to be:

$$\langle V\rangle_{ring,1} \approx 2.7 - 3.0 \cdot \langle D\rangle_{lig}^3. \tag{2}$$

Assuming each ring contributes on average only by half of its volume, since the rings are interconnected, the mean ring volume might also be estimated from half the mean volume of a torus with mean ligament and ring radii $\langle R\rangle_{lig}$ and $\langle R\rangle_{ring}$ as:

$$\langle V\rangle_{ring,2} \approx \left(\pi \cdot \langle R\rangle_{lig}\right)^2 \cdot \langle R\rangle_{ring}. \tag{3}$$

Equating eqns. (2) and (3) yields a linear dependency of the mean ring diameter $\langle D\rangle_{ring}$ with respect to the mean ligament diameter $\langle D\rangle_{lig}$:

$$\langle D\rangle_{ring} \approx 2.2 - 2.4 \cdot \langle D\rangle_{lig}. \tag{4}$$

This indicates that a single parameter is sufficient to fully characterize the structural sizes of the npg samples used in this investigation.

Since also a linear dependency of $|\langle\kappa_1\rangle|^{-1}$ with respect to $\langle D\rangle_{lig}$ was found (see Fig 10), the mean ring diameters can be expressed roughly through the inverse mean κ_1:

$$\langle D\rangle_{ring} \approx 0.8 \cdot \left|\left\langle \kappa_1 \right\rangle\right|^{-1}. \tag{5}$$

Note that the $\langle\kappa_1\rangle$<0 for all samples.

Clearly, this result assumes that the rings are built up by the whole solid material available, thus ignoring existing dead-end ligaments and the interconnecting parts that can strongly alter the torus volume calculations (but not the connectivity density). Consequently, the analysis given above should take into account an effective solid volume fraction ρ_{eff}=$C \cdot \rho_{solid}$, with C being a positive constant smaller than 1. We recently showed that an effective load-bearing solid volume fraction can be defined, which is significantly lower than the total volume fraction [7].

4. Summary

In summary, we have shown that through the use of FIB-based tomography applied to representative volumes, the salient structural parameters can be identified in terms of the mean principle curvatures. An analysis based on an ideal torus provided insight into the influences of ellipticity and ligament diameter variability of the fundamental ring-like structure of the npg network. We have emphasized the importance of addressing the comparability of results from various structural investigations of npg; the influence

of sample preparation, especially the dealloying approach, the validity of considering the analyzed material volume as representative, and the potential artifacts of any experiment and subsequent analysis made, can all influence the conclusions made. The issue of representative volumes has been invoked as the likely reason our conclusions regarding self similar coarsening are in strong disagreement by those made by others. We conclude that the inverse mean principle curvatures relate directly to physical dimensions associated with the ligament network structure, namely the mean ligament diameter and the diameter of an effective ring structure supporting load. Since both measures directly scale with the mean ligament diameter, one parameter is sufficient to fully characterize the microstructure of the npg system investigated. Furthermore, despite certain discrepancies, the result support a view of npg coarsening which, depending on the purpose, might be considered sufficiently self similar.

Acknowledgement

This work was funded by the German Research Foundation (DFG) through SFB 986 ″Tailor-Made Multi-Scale Materials Systems - M^{3}″, projects B4 and B2.

References

[1] G. Gottstein, Materialwissenschaft und Werkstofftechnik, Springer, 2014.
[2] H. Atkinson, Theories of normal grain growth in pure single phase systems, Acta Metall. 36 (1988) 469–491.
[3] P. Voorhees, The theory of ostwald ripening, J. Stat. Phys. 38 (1985) 231–252.
[4] L. Qian, M. Chen, Ultrafine nanoporous gold by low-temperature dealloying and kinetics of nanopore formation, Appl. Phys. Lett. 91 (2007) 083105.
[5] K. Kolluri, M. Demkowicz, Coarsening by network restructuring in model nanoporous gold, Acta Mater. 59 (2011) 7645–7653.
[6] Y. Kwon, K. Thornton, P. Voorhees, The topology and morphology of bicontinuous interfaces during coarsening, EPL 86 (2009) 46005.
[7] K. Hu, M. Ziehmer, K. Wang, E. Lilleodden, Nanoporous gold: 3D structural analyses of RVEs and their implications on scaling relations of mechanical behavior, Phil. Mag. Accept. (2016), http://dx.doi.org/10.1080/14786435.2016.1222087.
[8] Y. Chen-Wiegart, S. Wang, Y. Chu, W. Liu, I. McNulty, P. Voorhees, D. Dunand, Structural evolution of nanoporous gold during thermal coarsening, Acta Mater. 60 (2012) 4972–4981.
[9] Y. Kwon, K. Thornton, P. Voorhees, Coarsening of bicontinuous structures via nonconserved and conserved dynamics, Phys. Rev. E 75 (2007) 021120.
[10] D. Kammer, P. Voorhees, The morphological evolution of dendritic microstructures during coarsening, Acta Mater. 54 (2006) 1549–1558.
[11] T. Hildebrand, P. Rüegsegger, A new method for the model-independent assessment of thickness in three-dimensional images, J. Microsc. 185 (2009) 67–75.
[12] J. Schindelin, I. Arganda-Carreras, E. Frise, et al., Fiji: an open-source platform for biological-image analysis, Nat. methods 9 (2012) 676–682.
[13] K. Wang, J. Weissmüller, Composites of nanoporous gold and polymer, Adv. Mater. 25 (2013) 1280–1284.
[14] F. Soldera, F. Lasagni, F. Mücklich, Nano characterization of structures by focused ion beam (FIB) tomography, in: F. Lasagni, A. Lasagni (Eds.), Fabrication and Characterization in the Micro-nano Range, Springer, Berlin Heidelberg, 2011, pp. 171–199.
[15] K. Mangipudi, V. Radisch, L. Holzer, C. Volkert, A FIB-nanotomography method for accurate 3D reconstruction of open nanoporous structures, Utramicroscopy 163 (2016) 38–47.
[16] Y. Nishikawa, H. Jinnai, T. Koga, T. Hashimoto, S. Hyde, Measurements of interfacial curvatures of bicontinuous structure from three-dimensional digital images. 1. A parallel surface method, Langmuir 14 (1998) 1242–1249.
[17] H. Jinnai, T. Koga, Y. Nishikawa, T. Hashimoto, S. Hyde, Curvature determination of spinodal interface in a condensed matter system, Phys. Rev. Lett. 78 (1997) 2248–2251.
[18] I. Bronstein, K. Semendjajew, Taschenbuch der Mathematik, Harri Deutsch, 1987.